Supporting Material

From Static Structure to Living Protein:
Computational Analysis of Cytochrome *c* Oxidase Main-chain Flexibility

Leann Buhrow, Shelagh Ferguson-Miller, and Leslie A. Kuhn

Supporting Materials and Methods

ProFlex Analysis of Intrinsic Protein Flexibility

ProFlex calculates a hydrogen-bond dilution profile (1). To calculate the profile, the protein's hydrogen bonds are broken one by one, from weakest to strongest (according to the potential energy formula described below), and the constraint counting algorithm is run after each bond is broken. This simulates incremental thermal denaturation of the structure, as the calculated temperature rises and hydrogen bonds weaker than the current energy level are broken. The protein commonly appears as a single large rigid region when the simulated temperature is low and weak hydrogen bonds and salt bridges are included. The structure then gradually breaks into two or more rigid regions (often corresponding to the known native state), before going through a cooperative phase transition to a completely flexible chain as the simulated temperature rises (2). Hydrophobic interactions are maintained throughout the process, as their strength actually increases somewhat with modest increases in temperature (3).

There is no single energy level that corresponds to the native state of all proteins, in terms of rigid and flexible regions. This may result from the different experimental conditions and force fields under which protein structures are determined. Because our goal is to analyze flexibility on a global scale, e.g., between domains, we analyze proteins at an energy level in which the structure contains at least two rigid domains of substantial size (20 or more residues). This typically occurs when the protein has just relaxed from a single large rigid cluster into two clusters. Rigid clusters of at least 20 residues typically correspond to supra-secondary structures (e.g., two packed helices, rather than one long helix), while smaller rigid clusters do not. This choice of energy level for analysis has been shown to predict internal regions of flexibility and hinge residues well (4). Defining the energy level effectively defines the set of hydrogen bonds and salt bridges to include as non-covalent interactions (constraints), which are then used by ProFlex to evaluate the relative flexibility of different regions in the protein by using a constraint-counting approach as described in (5).

All ProFlex input crystal structures have hydrogen atom positions added prior to beginning the method in order to identify hydrogen bonds and salt bridges with good geometry and favorable energy. Hydrogen atom positions and partial charges (for salt bridge identification) were assigned using WhatIf (version 6) for protein and water atoms and InsightII with CVFF parameters for heme groups. This method selects positions for hydrogen atoms that optimize the energetic favorability of the resulting hydrogen-bond network. WhatIf considers bond lengths of all possible donor-acceptor, donor-hydrogen, and hydrogen-acceptor atoms and the bond angle between the proton donor-hydrogen-

acceptor to maximize the number of hydrogen bonds with an input structure. Protonatable groups with fixed geometry become protonated 1.0 Å from the donor atom, while in donor groups with rotational degrees of freedom (e.g., terminal protons on a hydroxyl or lysine side chain), the hydrogen is placed 1.0 Å from the donor atom at all low energy conformations and in the acceptor atom's plane. The configuration is kept that maximizes the number of resulting hydrogen bonds and salt bridges. ProFlex calculates hydrogen bond energies by:

$$E_{HB} = V_0 \left\{ 5 \left(\frac{R_0}{R} \right)^{12} - 6 \left(\frac{R_0}{R} \right)^{10} \right\} F(\theta, \phi, \gamma),$$

where R is the donor to acceptor atom distance, θ is the donor-hydrogen-acceptor atom angle, ϕ is the hydrogen-acceptor-acceptor bonded atom angle, and γ is the out of plane angle created with sp2 hybridization (5). ProFlex identifies and ranks all hydrogen bonds in terms of energy using the above formula, with more negative values reflecting stronger, more favorable interactions. The hydrogen bond dilution profile (Supporting Figure 1) is used visualize the change in flexibility upon successive removal of the weakest hydrogen bonds, thereby estimating thermal denaturation.

Supporting Tables

Supporting Table 1: C*c*O structures analyzed by *ProFlex* and *elNémo*				
PDB Entry	Description	Source	Resolution (Å)	R-Factor (R-Free)
2GSM (6)	Two-subunit oxidized aa_3 oxidase	*R. sphaeroides*	2.00	0.214 (0.232)
3FYE (7)	Two-subunit reduced aa_3 oxidase	*R. sphaeroides*	2.15	0.196 (0.221)
1M56 (8)	Four-subunit aa_3 oxidase	*R. sphaeroides*	2.30 / 2.69	0.236 (0.275)
1AR1 (9)	Two-subunit with antibody F_v fragment	*P. denitrificans*	2.70	0.207 (0.261)
1XME (10)	Recombinant Cytochrome ba_3 oxidase	*T. thermophilus*	2.30	0.217 (0.236)

High resolution two and four subunit structures from *R. sphaeroides*, *P. denitrificans,* and *T. thermophilus* were selected for flexibility and low energy motion analysis using *ProFlex* and *elNémo*. For the *R. sphaeroides* structures, one biological unit was selected from each unit cell, with chain identifiers A and B for two-subunit structures or A-D for four-subunit structures. The *P. denitrificans* structure was studied in the absence of the co-crystallized antibody F_v fragment, using subunits I and II (chain identifiers A and B). The three-subunit *T. thermophilus* structure (chains A, B, and C), analogous to the *Rs*C*c*O and *Pd*C*c*O two-subunit structures, was also studied. All analyzed structures are in the oxidized state except for the two-subunit reduced *Rs*C*c*O structure. For PDB structural references, please see the citation section at the end of this document.

Supporting Table 2: Comparison of oxidized and reduced two-subunit *RsCcO* structures

	Oxidized (6)	Dithionite Reduced (7)
Space Group	P $2_12_12_1$	P $2_12_12_1$
Cell Dimensions	a=125.0 b=131.6 c=176.8	a=124.6 b=131.5 c=176.2
Molecules per Asymmetric Unit	2	2
Resolution Range (Å)	20-2.0	50-2.15
Completeness (%)	96.1	99.1
Number of Unique Reflections	184,839	151,414
Redundancy	4.5	4.6
R_{merge} (%)	6.0	6.5
I/σ	14.8	20.8
Number of Refined Atoms	13,648	13,615
R-Factor/R-Free (%)	21.4/23.2	19.6/22.1
Average B-Factor	36.5	45.8
RMSD Bond Length (Å)	0.013	0.012
RMSD Bond Angle (°)	1.253	1.227
RMSD (Å) Between Structures	0.219 (1429 atoms aligned to 1429 atoms)	

The oxidized and reduced structures of *RsCcO* are substantially similar, as they were solved using the same method by the same research group (6-7). The generation of reduced crystals was accomplished by soaking oxidized crystals in a stabilizing solution, which included 10mM sodium dithionite, prior to flash cooling and data collection. The reduced structure shows significant displacement of the heme a_3 porphyrin ring and farnesyl tail, movement of subunit I helix VIII, which contains critical K-pathway residues, and the resolution of additional K-pathway water molecules (7). Analyses of these structures using *ProFlex* and *elNémo* methods are considerably similar despite the slight loss of resolution for the reduced structure.

Supporting Table 3: Diverse membrane protein folds analyzed by *ProFlex* and *elNémo*

PDB Entry	Description	Source	Resolution (Å)	R-Factor (R-Free)
2RH1 (11)	β2 adrenergic receptor	*Homo sapiens*	2.4	0.20 (0.23)
1K4C (12)	Potassium channel KcsA-Fab complex	*Streptomyces lividans*	2.0	0.22 (0.23)
3EMN (13)	Voltage-dependent anion channel	*Mus musculus*	2.3	0.24 (0.28)

To directly compare low energy motions of membrane proteins, we have analyzed a G-protein coupled receptor: the β2 adenergic receptor, the α-helical KcsA potassium channel, and a β-barrel transporter protein: the voltage-dependent anion channel (VDAC). These proteins were selected as they represent diverse integral membrane proteins, have available crystal structures of similar resolution to that of the analyzed C*c*O structures, and have been studied in terms of conformational change or dynamics required for function.
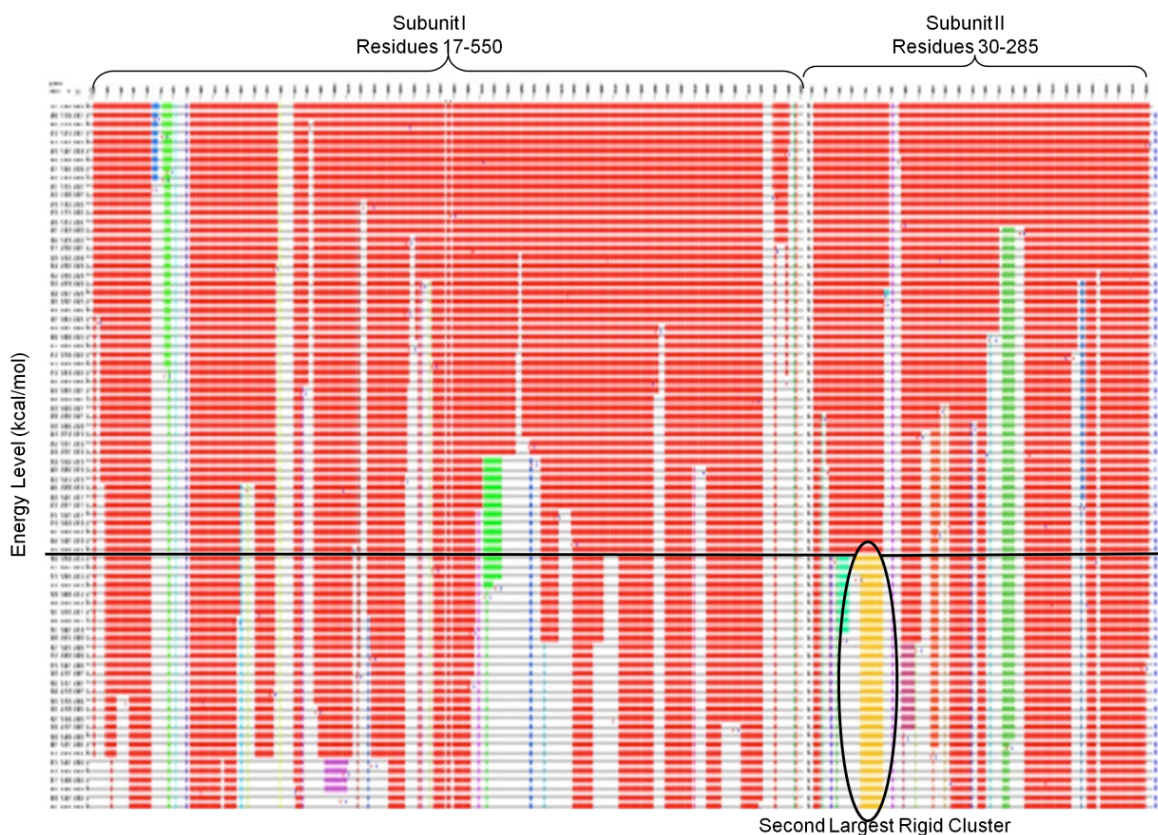
	RsCcO		β₂ adrenergic receptor		KcsA potassium channel		Voltage-dependent anion channel	
	Displaced Atoms (%)	Relative Frequency	Displaced Atoms (%)	Relative Frequency	Displaced Atoms (%)	Relative Frequency	Displaced Atoms (%)	Relative Frequency
Mode 7	47	1.00	71	1.00	50	1.00	46	1.00
Mode 8	47	1.04	58	1.25	68	1.44	53	1.09
Mode 9	38	1.08	68	1.46	68	1.44	67	1.28

Supporting Table 4: *elNémo* percentage of atoms significantly displaced and relative frequencies of normal modes

The low energy motions generated by *elNémo* are given as relative amplitudes in the direction of maximum displacement for a given frequency or normal mode. The amplitudes are automatically normalized relative to an arbitrarily specified maximum displacement, only relative values can be analyzed within a given structure and cannot be compared between simulations done for different proteins. However, it is possible to compare the percentage of atoms with significant motion in a given protein at a given frequency, called the "collectivity" in *elNémo* literature (14). Values approaching 1.0 signify global motion of the entire protein, while values approaching 0.0 signify localized motion. In the two lowest energy modes, modes 7 and 8, the percentage of atoms displaced in CcO is consistent with those of the KscA potassium channel and VDAC with about 50% of atoms being significantly displaced. The additional mobility of β₂ adrenergic receptor (71% of atoms displaced in the mode 7) may be due to the protein sampling of active protein conformations in the absence of agonists (11). As the frequencies of CcO are internally normalized, the motions observed in a given frequency cannot be compared directly to the rate of oxygen access or proton pumping. However, normal mode analysis of ion channels have observed biological main-chain conformational changes occurring on the millisecond timescale (15-18). Observed CcO motions in the current *elNémo* analysis may also occur on the millisecond timescale, consistent with the protein's reaction cycle.

Supporting Table 5 (next page). Relative magnitudes of helix tilting, elongation, and internal conformational change were measured by comparing the two extreme structural snapshots from the trajectory for each of the three lowest-frequency *elNémo* modes. In order to measure helical tilt angles, each helix was represented by two line segments connecting the Cα at each helix end with the central most stationary residue in the helix. Stationary residues and mean displacement $<R^2>$ are defined as in the *elNémo* section of the Methods. Helical tilting was measured by the minimum angle change of the helix on either side of the membrane, to offset the additional angular effect of bending in some helices. Internal conformational changes were measured by calculating the root mean squared displacement (RMSD) of the helix Cα's between the extreme conformations in each mode. Helical length change was determined as the difference in distance between the helix terminal Cα's between the extreme conformations. Measurements deviating by more than one standard deviation above or below the mean value for all helices appear in boldface are indicated by "^" or "v", respectively, whereas "^^" or "vv" indicates two standard deviations above/below the mean.

Supporting Table 5: C*c*O helical conformational changes in *elNémo* low-energy modes

| Mode	Helix	Stationary Residue(s)	$\langle R^2 \rangle$	Helical Tilt (º)	Conformational Change (RMSD, Å)	Length Change (Å)
7	I_I	$S44_I$-$V45_I$	3.4×10^{-3}	2.45	**1.042^**	0.740
	II_I	$H127_I$	2.2×10^{-3}	5.51	0.406	0.170
	III_I	$L152_I$	2.3×10^{-3}	5.06	**0.316_V**	0.520
	IV_I	$I191_I$	1.3×10^{-3}	5.44	**0.274_V**	0.250
	V_I	$I250_I$	1.0×10^{-3}	4.87	0.436	0.610
	VI_I	$A294_I$	6.0×10^{-4}	2.78	0.676	**0.14_V**
	VII_I	$V329_I$	2.4×10^{-3}	1.73	0.357	1.000
	$VIII_I$	$T352_I$-$A356_I$	3.6×10^{-3}	4.58	0.468	**0.00_V**
	IX_I	$F391_I$	7.0×10^{-4}	**1.13_V**	0.454	0.200
	X_I	$A427_I$-$V428_I$	1.2×10^{-3}	5.41	0.421	0.840
	XI_I	$G463_I$	1.6×10^{-3}	3.21	0.999	**2.64^**
	XII_I	$L503_I$	2.1×10^{-3}	5.46	**1.37^^**	**2.98^**
	I_{II}	$I68_{II}$	1.4×10^{-3}	**6.09^**	**0.25_V**	**2.7^**
	II_{II}	$I111_{II}$	3.4×10^{-3}	3.97	**0.25_V**	**2.44^**
8	I_I	$S44_I$ - $V45_I$	3.4×10^{-3}	4.44	0.822	**2.47^**
	II_I	$G101_I$ & $H127_I$	2.2×10^{-3}	**8.31^^**	0.850	0.970
	III_I	$L152_I$	2.3×10^{-3}	**5.94^**	0.794	**0.15_V**
	IV_I	$I191_I$	1.3×10^{-3}	3.28	**1.055^**	**2.22^**
	V_I	$I250_I$	1.0×10^{-3}	**0.26_V**	0.996	1.500
	VI_I	$Y275_I$ & $A294_I$	6.0×10^{-4}	3.16	0.779	0.760
	VII_I	$V329_I$	2.4×10^{-3}	**1.24_V**	0.682	1.640
	$VIII_I$	$A351_I$ - $A356_I$	3.6×10^{-3}	**9.56^^**	0.878	**2.95^**
	IX_I	$F391_I$	7.0×10^{-4}	**7.28^**	**0.317_V**	0.910
		$A427_I$-$V428_I$	1.2×10^{-3}	**1.12_V**	**0.321_V**	**0.16_V**
	XI_I	$G463_I$	1.6×10^{-3}	3.68	**0.325_V**	0.280
	XII_I	$L503_I$	2.1×10^{-3}	5.35	0.484	**0.03_V**
	I_{II}	$I68_{II}$	1.4×10^{-3}	4.69	**1.333^**	1.010
	II_{II}	$I111_{II}$	3.4×10^{-3}	5.26	**1.229^**	1.630
9	I_I	$G37_I$	7.5×10^{-3}	1.67	0.687	1.130
	II_I	$L115_I$ -$F116_I$	2.3×10^{-3}	3.49	0.777	0.970
	III_I	$S142_I$	7.0×10^{-3}	2.77	0.703	**4.26^^^**
	IV_I	$I209_I$	1.8×10^{-3}	3.33	0.540	**2.22^**
	V_I	$I232_I$	1.4×10^{-3}	2.09	0.468	1.500
	VI_I	$P293_I$	6.0×10^{-4}	2.07	0.503	0.760
	VII_I	$M320_I$-$V321_I$	4.5×10^{-3}	**1.27_V**	0.504	1.660
	$VIII_I$	$T359_I$ & $K362_I$	5.6×10^{-3}	2.26	0.786	1.460
	IX_I	$W383_I$	1.4×10^{-3}	**1.01_V**	0.523	**0.06_V**
	X_I	$A434_I$	1.3×10^{-3}	3.10	0.418	**0.16_V**
	XI_I	$K454_I$	8.0×10^{-4}	2.40	0.549	1.050
	XII_I	$E488_I$	5.0×10^{-3}	**0.00_V**	0.874	**0.03_V**
	I_{II}	$L62_I$	6.1×10^{-3}	2.99	**1.352^^**	0.5
	II_{II}	$Q127_I$	6.2×10^{-3}	**0.00_V**	**1.42^^**	1.63

Supporting Figures

Supporting Figure 1: Dependence of C*c*O flexibility on thermal energy increase, analyzed by *ProFlex* hydrogen bond dilution profiles. These profiles indicate the rigid and flexible regions of the protein backbone by residue number along the x-axis, with change in energy along the y-axis. At the top of the y-axis, the energy is 0 kcal/mol, descending to increasingly negative values (corresponding to thermal energy), at which only the strongest hydrogen bonds and salt bridges remain. Flexible regions appear as thin gray lines along the x-axis, while each mutually rigid region of main chain appears as a colored bar; different colors represent independently rigid regions. For each energy at which the protein becomes more flexible, a new line (representing the new rigid decomposition) is drawn in the profile. Here, the *ProFlex* hydrogen bond dilution profile of the reduced *Rs*C*c*O crystal structure (PDB entry 3FYE (7)) is depicted. *ProFlex* comparisons between different bacterial structures in the Results are based upon selecting the thermal energy for each at which the second largest rigid cluster (shown in yellow bars) is maximal in size (number of atoms).
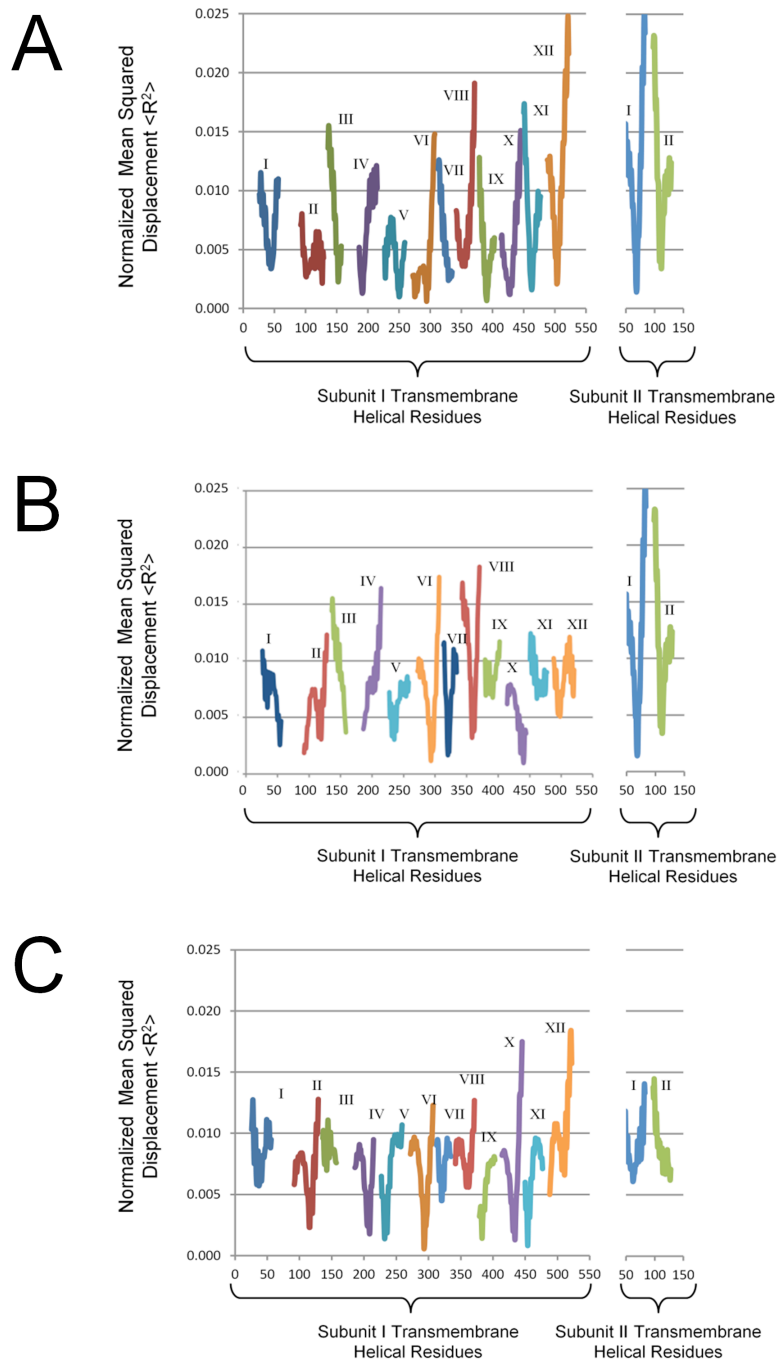
Supporting Figure 2: Mean squared displacement values within *Rs*C*c*O transmembrane helices. C_α motions in *elNémo* (A) mode 7, (B) mode 8, and (C) mode 9 are graphed as a function of helix residue numbers (PDB entry 2GSM (6)), with helices individually colored and labeled. The stationary point in each helix, defined as the residue(s) undergoing least displacement, appears as a minimum in the $<R^2>$ values. Large displacements of helix termini reflect tilting, bending and compression motions.

7
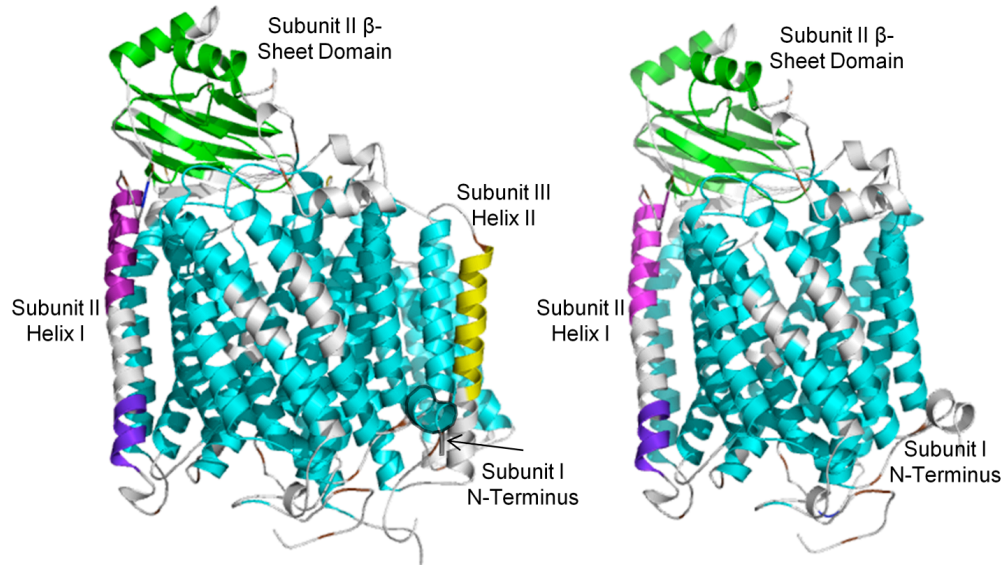
Supporting Figure 3: *ProFlex* **flexibility comparison the of two and four subunit crystal structures of *Rs*CcO.** (A) The four-subunit structure of *Rs*CcO (PDB entry 1M56 (8)) was analyzed with *ProFlex* to evaluate the influence of subunits III-IV on the catalytic core flexibility (subunits I-II). This structure has lower resolution in the direction perpendicular to the membrane and fewer defined water molecule positions at the subunit I-II interface relative to the available two-subunit structures. (B) When subunits III-IV are removed from the four-subunit structure to analyze subunits I-II alone, the catalytic core is observed to have very similar flexible regions to those seen in the presence of subunits III-IV (panel A). An exception is the short N-terminal helix of subunit I appears rigid in the four-subunit structure (colored blue as part of the core rigid region in panel A), whereas in the structure with subunits III and IV removed (B), it becomes flexible.
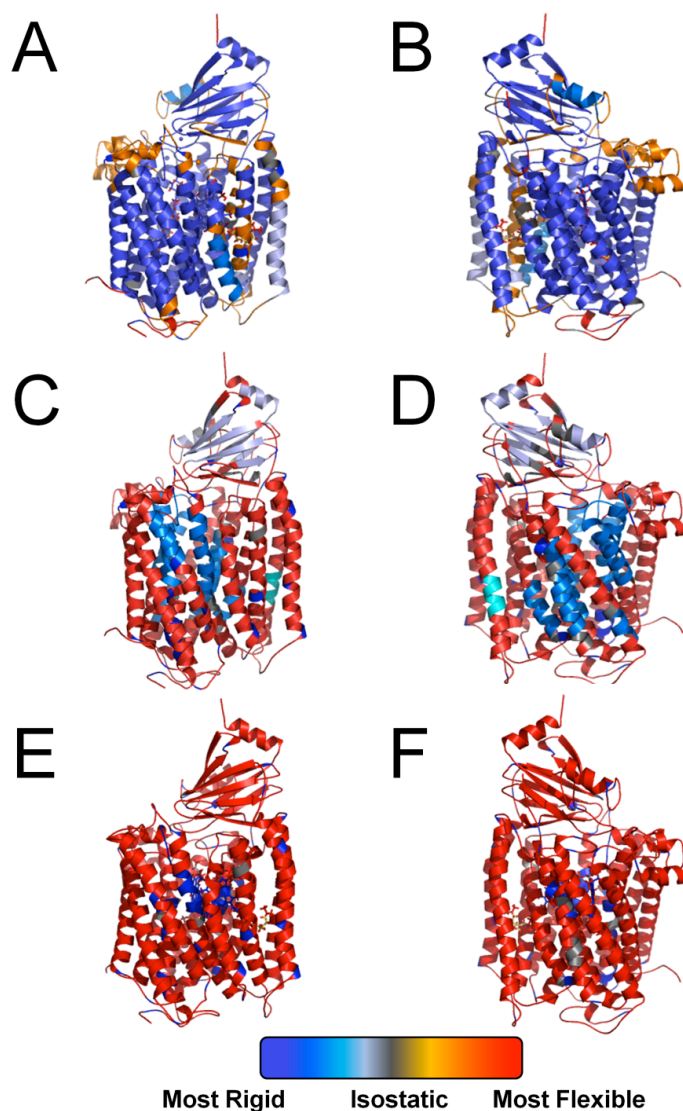
Supporting Figure 4: Thermal denaturation of the *RsCcO* structure by *ProFlex*. As the energy increases from top to bottom in these panels (with the right view in each pair rotated by 180° about the vertical axis), *ProFlex* recalculates the internal flexibility. A gradient from gray to light blue to deep blue indicates increasing rigidity, while a gradient from yellow to red indicates increasing flexibility. (A and B) At the initial analyzed energy (-2.938 kcal/mol), *RsCcO* (PDB entry 2GSM (6)) is composed of a rigid core of helices I-VI, X-XII and the subunit II β-sheet domain. Helices VII-VIII surrounding the K-pathway show the greatest transmembrane flexibility, with central hinges connecting stable helical ends which can undergo rigid-body motion. The cytochrome *c* interaction site and subunit I and II C-termini are the most flexible regions outside the membrane. (C and D) At higher but still moderate energy (-4.248 kcal/mol), all helices except for those nearest the heme groups (II, VI, and X) attain significant flexibility, while the β-sheet domain remains barely stable. (E and F) At the highest sampled energy (-7.645 kcal/mol), *RsCcO* becomes a flexibly coupled structure surrounding the heme groups.

9

Supporting Figure 5 (next page): ***Rs*C*c*O, β₂ adrenergic receptor, KcsA potassium channel, and VDAC residue displacement.** Structural details for input structures can be found in Supporting Table 3. Displacements of residue in modes 7 (panels A, E, I, and M), 8 (panels B, F, J, and N), and 9 (panels C, G, K, and O) are colored spectrally, where blue is the most stationary and red is the most displaced. To compare these results to C*c*O displacements (Manuscript Figure 4A), the most mobile and least mobile residues in the three lowest energy modes were defined (panels D, H, L, and P). Three or more consecutive residues undergoing displacement of one standard deviation above or below the average displacement in the three lowest energy modes are colored orange and blue, respectively, while three or more consecutive residues undergoing displacements greater than two standard deviations above the average are colored red.
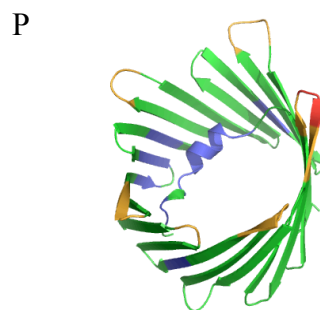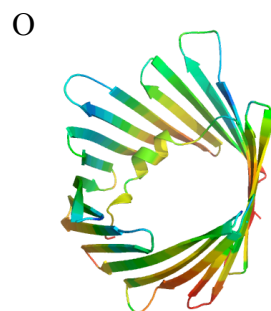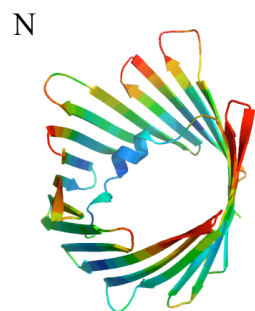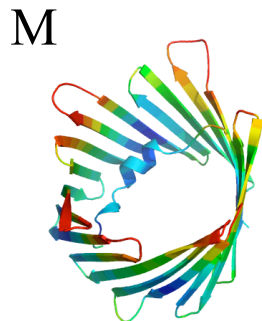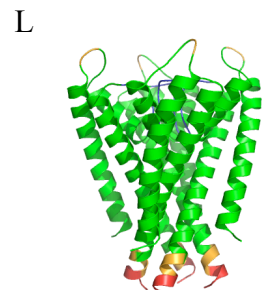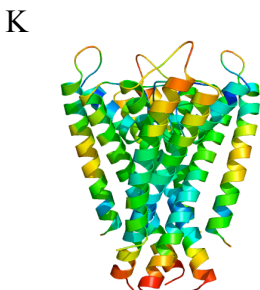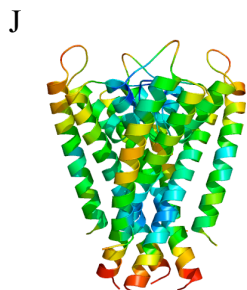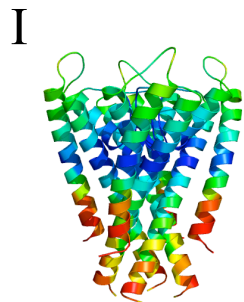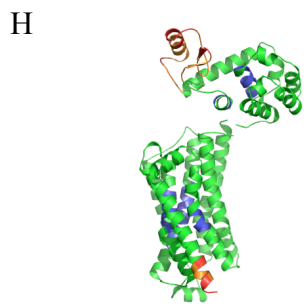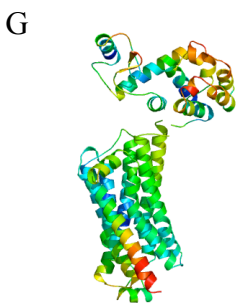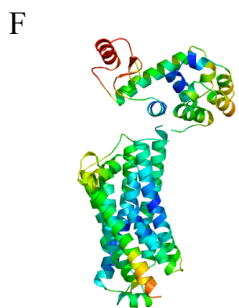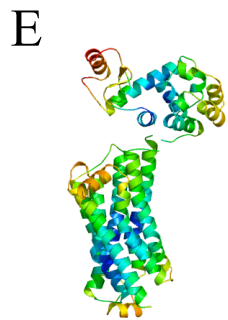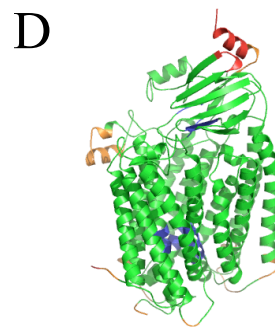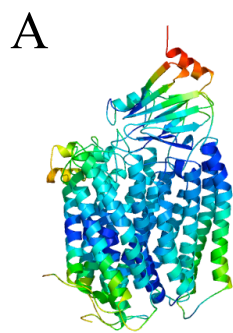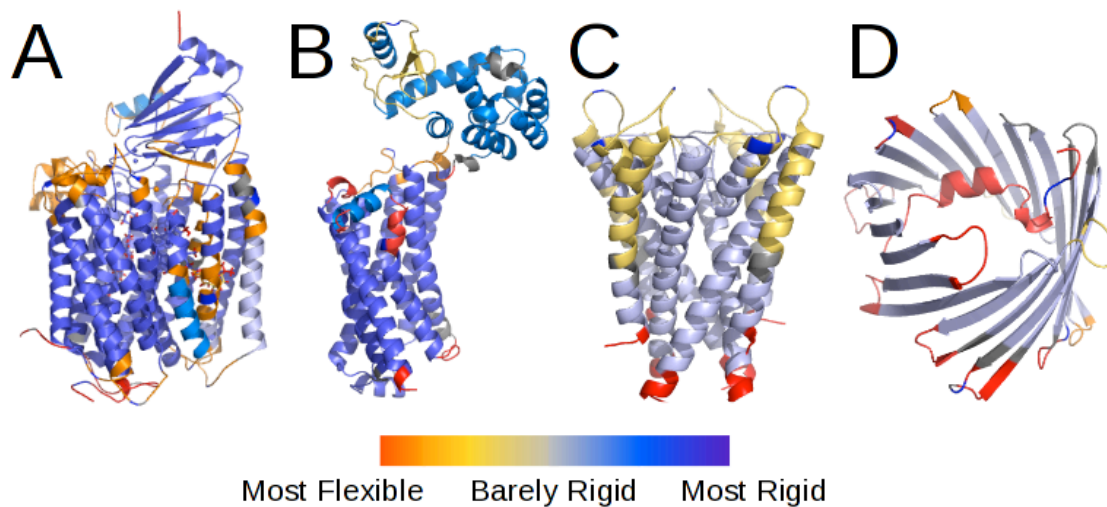
Supporting Figure 6: Relative flexibility of membrane proteins assessed using *ProFlex*.
(A) *Rs*C*c*O, (B) β$_2$ adrenergic receptor, (C) KcsA potassium channel, and (D) voltage-dependent anion transporter were analyzed using *ProFlex* (Structural details can be found in Supporting Table 3). The proteins are represented as ribbon diagrams and colored by degree of rigidity, from blue for highly rigid regions, to gray for barely rigid regions, to red for highly flexible regions.
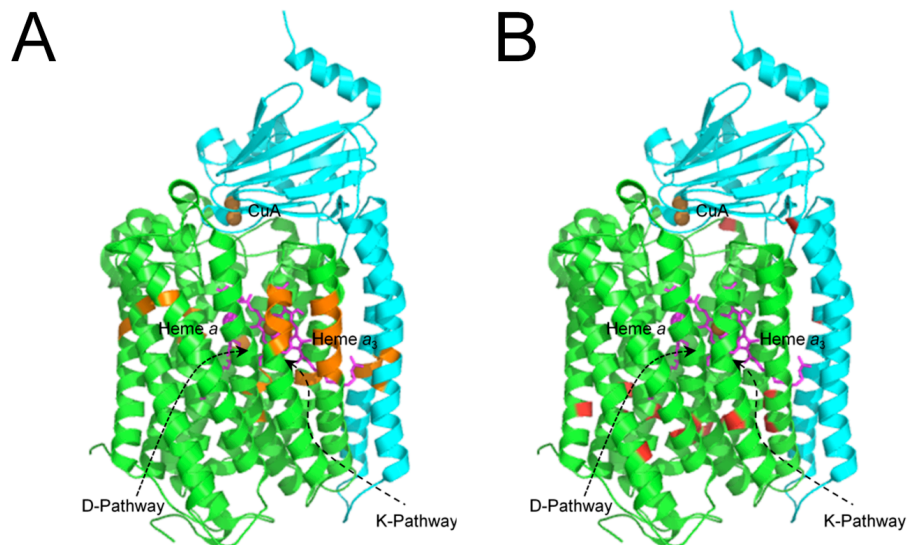
Supporting Figure 7: Planes of relatively stationary residues in the C*c*O transmembrane helices. *Rs*C*c*O (PDB code 2GSM (6)) subunits I and II are colored green and cyan, respectively. Heme cofactors are represented by magenta tubes, and copper A, magnesium, and copper B appear as copper or lime colored spheres. The most stationary helical residues, based on *elNémo* normalized mean squared displacement ($<R^2>$) values (Supporting Table 5), appear in (A) orange for modes 7 and 8 (in which overlapping sets of residues were stationary) and (B) red for mode 9.

Supporting Animations

***ElNémo* low-energy motions about the equilibrium conformation of C*c*O (PDB entry 2GSM (6)).**
These animations cycle through the 11 conformational snapshots saved for each of the three lowest-frequency normal modes, centered on the crystallographic conformation. Subunits I and II are depicted as green and cyan ribbons, respectively, while heme cofactors are represented as magenta tubes. Regions of the protein are highlighted. The highly flexible subunit I C-terminus is colored red, the pontoon helix is colored orange, the interfacially coupled regions of subunits I and II (helix VII-VIII loop, the ends of helix IX and subunit II helices I-II, and the subunit II β-strand) are colored yellow, the subunit I helix III-IV loop is in dark cyan, the K-pathway is colored blue with critical residues shown in sticks, and the D-pathway is represented in dark purple with critical residues shown in stick diagram. The animation can be viewed in a media player such as QuickTime that reads .mov files. To view the cycle of motions more than once, select the "loop back and forth" option located under the View or Movie menu.

Movie 1: The lowest frequency internal motions, corresponding to mode 7, show counter-rotational twisting on the interior and exterior of the membrane. The protein located near the inside of the membrane rotates about an axis perpendicular to the membrane plane, whereas on the outside of the membrane, the protein rotates about an axis tilted by ~30º, parallel to the subunit II β-strands.

Movie 2: The next lowest-frequency mode, 8, involves counter-rotational motions of C*c*O on each side of the membrane about an axis perpendicular to the membrane plane.

Movie 3: The third lowest-frequency mode, 9, shows a C-clamp-like compression and expansion of subunits I and II, in which the pontoon helix near the outside membrane surface of the protein approaches the subunit I C-terminus on the inside of the protein.

Supporting Citations

1. Hespenheide, B. M., A. J. Rader, M. F. Thorpe, and L. A. Kuhn. 2002. Identifying protein folding cores from the evolution of flexible regions during unfolding. J. Mol. Graph. Model. Graphics. 21:195-207.

2. Rader, A. J., B. M. Hespenheide, L. A. Kuhn, M. F. Thorpe. 2002. Protein unfolding: Rigidity lost. Proc. Natl. Acad. Sci. USA 99: 3540-3545.

3. Tanford, C. 1980. The hydrophobic effect. Wiley, New York.

4. Keating, K. S., S. C. Flores, M. B. Gerstein, and L. A. Kuhn. 2008. StoneHinge: Hinge prediction by network analysis of individual protein structures. Protein Science. 18: 359-371.

5. Jacobs, D. J., A. J. Rader, L. A. Kuhn, and M. F. Thorpe. 2001. Protein flexibility predictions using graph theory. Proteins. 44:150-165.

6. Qin, L., C. Hiser, A. Mulichak, R. M. Garavito, and S. Ferguson-Miller. 2006. Identification of conserved lipid/detergent-binding sites in a high-resolution structure of the membrane protein cytochrome *c* oxidase. Proc. Natl. Acad. Sci. USA. 103:16117-16122.

7. Qin, L., J. Liu, D. A. Mills, D. A. Proshlyakov, C. Hiser, and S. Ferguson-Miller. 2009. Redox-dependent conformational changes in cytochrome *c* oxidase suggest a gating mechanism for proton uptake. Biochemistry. 48:5121-5130.

8. Svensson-Ek, M., J. Abramson, G. Larsson, S. Törnroth, P. Brzezinski, and S. Iwata. 2002. The x-ray crystal structures of wild-type and EQ (I-286) mutant cytochrome *c* oxidases from *Rhodobacter sphaeroides*. J. Mol. Biol. 321:329-339.

9. Ostermeier, C., A. Harrenga, U. Ermler, and H. Michel. 1997. Structure at 2.7 Å resolution of the *Paracoccus denitrificans* two-subunit cytochrome *c* oxidase complexed with an antibody F_V fragment. Proc. Natl. Acad. Sci. USA. 94:10547-10553.

10. Hunsicker-Wang, L. M., R. L. Pacoma, Y. Chen, J. A. Fee, and C. D. Stout. 2005. A novel cryoprotection scheme for enhancing the diffraction of crystals of recombinant cytochrome ba_3 oxidase from *Thermus thermophilus*. Acta Cryst. D61:340-343.

11. Rasmussen, S. G. F., H.-J. Choi, J. J. Fung, E. Pardon, P. Casarosa, P. S. Chae, B. T. DeVree, D. M. Rosenbaun, F. S. Thian, T. S. Kobilka, A. Schnapp, I. Konetzki, R. K. Sunahara, S. H. Gellman, A. Pautsch, J. Steyaert, W. I. Weis, and B. K. Kobilka. 2011. Structure of a nanobody-stabilized active site of the β_2 adrenoceptor. Nature. 469:175-181.

12. Zhou, Y., J. H. Morais-Cabral, A. Kaufman, and R. MacKinnon. 2001. Chemistry of ion coordination and hydration revealed by a K+ channel-Fab complex at 2.0 Å resolution. Nature. 414: 43-48.

13. Ujwal, R., D. Cascio, J. P. Colletier, S. Faham, J. Zhang, L. Toro, P. Ping, J. Abramson. 2008. The crystal structure of mouse VDAC1 at 2.3 Å resolution reveals mechanistic insights into metabolic gating. Proc. Natl. Acad. Sci. USA. 105: 17742-17747.

14. Suhre, K., and Y.-H. Sanejouand. 2004. ElNémo: A normal mode web server for protein movement analysis and the generation of templates for molecular replacement. Nucleic Acids Res.

32:W610-W614.

15. Valadié, H., J. J. Lacapčre, Y.-H. Sanejouand, and C. Etchebest. 2003. Dynamical properties of the MscL of Escherichia coli: A normal mode analysis. J. Mol. Biol. 332:657-674.

16. Shrivastava, I. H., and I. Bahar. 2006. Common mechanism of pore opening shared by five different potassium channels. Biophys. J. 90:3929-3940.

17. Miloshevsky, G. V., and P. C. Jordan. 2006. The open state gating mechanism of gramicidin a requires relative opposed monomer rotation and simultaneous lateral displacement. Structure. 14:1241-1249.

18. Szarecka, A., Y. Xu, and P. Tang. 2007. Dynamics of heteropentameric nicotinic acetylcholine receptor: Implications of the gating mechanism. Proteins. 68:948-960.